Scilight

Materials and Sustainability
https://www.sciltp.com/journals/pc

Article

Unravelling the Formation of 2-Phenylethylammonium 2D Perovskites by *In Situ* GIWAXS

Valentin Munteanu [1], Ekaterina Kneschaurek [1], Lena Merten [1,2], Algirdas Dučinskas [3], Jovana Milić [3,4], Florian Bertram [5], Alexander Hinderhofer [1,6], Alexander Gerlach [1,7], Ivan Zaluzhnyy [1,6,*] and Frank Schreiber [1,6,*]

[1] Institut für Angewandte Physik, Universität Tübingen, Auf der Morgenstelle 10, 72076 Tübingen, Germany
[2] Division of Physical Chemistry, Lund University, Naturvetarvägen 14, 22100 Lund, Sweden
[3] Laboratory of Photonics and Interfaces, Institute of Chemical Sciences and Engineering, Ecole Polytechnique Fédérale de Lausanne, 1015 Lausanne, Switzerland
[4] Department of Chemistry, University of Turku, 20900 Turku, Finland
[5] Deutsches Elektronen-Synchrotron DESY, Notkestr. 85, 22607 Hamburg, Germany
[6] Center for Light-Matter Interaction, Sensors & Analytics LISA+, Universität Tübingen, Auf der Morgenstelle 15, 72076 Tübingen, Germany
[7] Institut für Physik, Universität Kassel, Heinrich-Plett-Str. 40, 34132 Kassel, Germany
* Correspondence: ivan.zaluzhnyy@uni-tuebingen.de (I.Z.); frank.schreiber@uni-tuebingen.de (F.S.)

How To Cite: Munteanu, V.; Kneschaurek, E.; Merten, L.; et al. Unravelling the Formation of 2-Phenylethylammonium 2D Perovskites by *In Situ* GIWAXS. *Materials and Sustainability* **2026**, *2*(2), 4. https://doi.org/10.53941/matsus.2026.100004

Received: 9 February 2026
Revised: 16 March 2026
Accepted: 23 March 2026
Published: 8 April 2026

Abstract: Hybrid lead halide perovskites are considered a highly promising material for future advancements of photovoltaic technologies due to their outstanding optoelectronic properties. Nevertheless, their instability under ambient conditions hinders the large-scale adoption of perovskite solar cells. Two-dimensional (2D) perovskites have been proposed to address the issue of instability, but these structures display anisotropic optoelectronic properties related to their layered structure. Moreover, their crystallization pathways are not well understood. Here we present insight into the crystallization process of 2-phenyethylammonium (PEA^+) Ruddlesden-Popper 2D perovskites with iodide (I^-) and bromide (Br^-) anions by performing *in situ* grazing incidence wide-angle X-ray scattering (GIWAXS) measurements of thin films with various compositions during their fabrication via spin-coating and thermal annealing. The GIWAXS data reveals the structure of coexisting 2D perovskite phases and their orientation with respect to the substrate for different precursor compositions. The bromide-based compositions exhibited crystallization already during spin-coating, while iodide-based compositions required thermal annealing to induce the crystallization process. For the latter ones, additional polymorphs were found, suggesting the intrinsic differences for compositions with different halides.

Keywords: 2D perovskites; *in situ* GIWAXS; crystallography

1. Introduction

Hybrid halide perovskite materials, ABX_3 where A is an organic cation (typically methylammonium (MA^+=$CH_3NH_3^+$) or formamidinium (FA^+=$NH_2CHNH_2^+$)), B is a metal cation (typically Pb^{2+}) and X is a halide anion (I^-, Cl^- or Br^-), have attracted a surge of interest from the scientific community over the last decade [1–6] due to their outstanding optoelectronic properties, such as high absorption coefficient [7], long charge carrier diffusion length [8], and low recombination rate [9]. These properties in conjunction with their potential low cost of fabrication [10] make them a prime active material for the next generation of solar cell devices [11]. Perovskite-based solar cells have made a huge progress in performance from the first reported power conversion efficiency of 3.8% [7] to the recently reported value of 26.7% [12]. A further advantage of perovskite solar cells is

their solution-based low temperature processing [13], which enables the use of flexible substrates, opening the possibility for fabricating wearable electronic devices [14], and using them in tandem solar cells [15].

Despite these achievements, the large-scale adoption of perovskite-based devices is hindered by their instability under environmental conditions. The exposure to oxygen and water leads to a quick degradation of the perovskite material [16, 17]. Two-dimensional (2D) perovskites [18–21] are a class of materials designed to combat these degradation mechanisms [22]. The intercalation of large organic spacer cations into the perovskite lattice results in the formation of a layered structure consisting of interconnected lead-halide octahedra layers separated by the organic spacer layers. Depending on the type of organic spacer cation two main classes of 2D perovskite structures emerge: Ruddlesden–Popper phase (double spacer layer for monofunctional spacers) or Dion–Jacobson phase (single spacer layer for bifunctional spacers) [23, 24]. It has been shown that this type of structure has a greatly enhanced resistance to humidity [25], due to the hydrophobicity of the bulky spacer cations. The number of stacked lead-halide octahedra layers defines the so-called dimensionality of the 2D perovskite n, as shown in Figure 1. The dimensionality n can be controlled by varying the stoichiometric ratio of the precursor components.

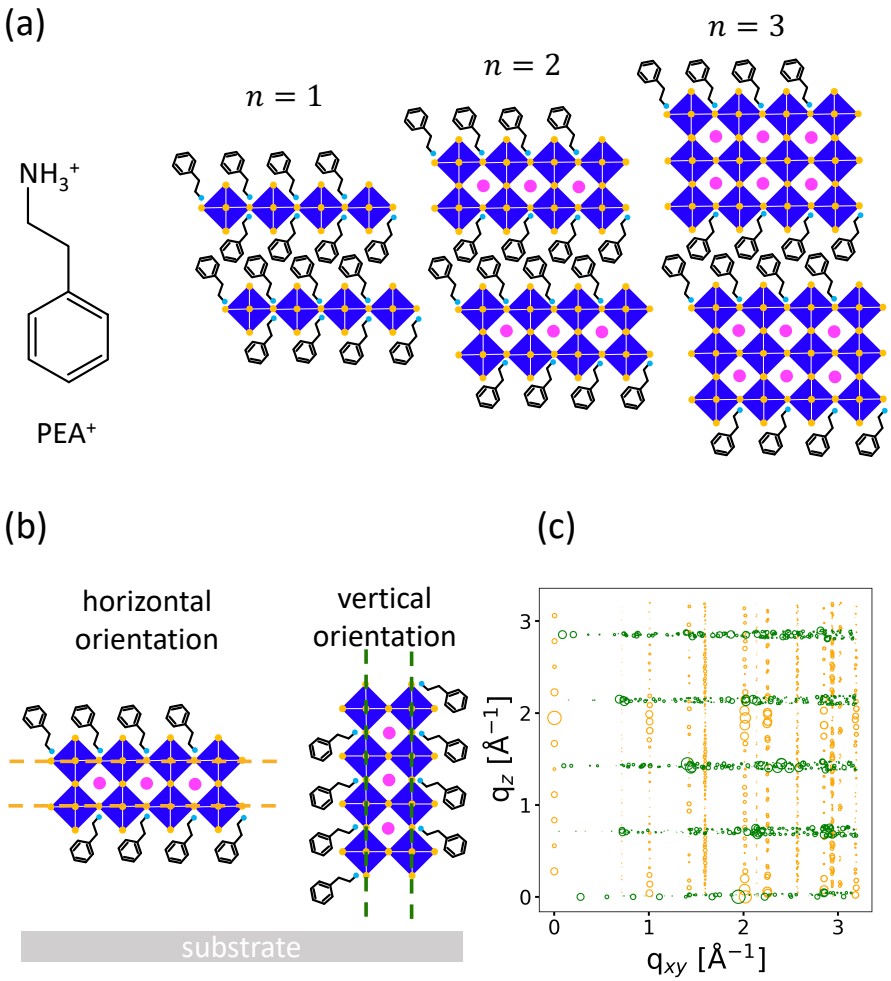

Figure 1. (**a**) Structure of the PEA^+ spacer and illustration of the corresponding Ruddlesden–Popper 2D perovskite phases with different dimensionalities n. (**b**) Orientation of the perovskite structures with respect to the substrate. The dashed lines show the possible propagation direction of the charge carriers: yellow for the horizontal orientation, green for the vertical orientation. Blue squares with yellow circles represent the lead-halide octahedra (PbI_6^{4-} or $PbBr_6^{4-}$), magenta circles—small organic cations (MA^+ or FA^+), and cyan circles—the amino groups of the PEA^+ cations. (**c**) Simulated diffraction pattern for $PEA_2MAPb_2I_7$ ($n = 2$) 2D perovskite in two orientations: yellow circles indicate the positions of the diffraction peaks for horizontal orientation and green circles—for vertical orientation. The size of the circles corresponds to the intensity of the peaks in GIWAXS.

As a consequence of the anisotropic structure causing anisotropic charge transport properties, the orientation of the 2D perovskites is a crucial aspect for their applications [26]. As shown in Figure 1b, only the structures with the vertical orientation with respect to the substrate allow the transport of charge carriers between the anode and cathode of solar cell devices. Previous studies have suggested that the formation of vertically oriented phases

is linked to nucleation from the liquid-air interface [27]. Still, the crystallization pathways of 2D perovskites are not well explored. This is further complicated by the fact that the synthesis of a 2D perovskite from a precursor solution generally results in a distribution of perovskite phases with different dimensionalities and orientations. Thus, synthesis of a 2D perovskite with a well-defined dimensionality n is extremely challenging [28], if feasible at all. Controlling the crystal morphology of fabricated perovskite thin films is essential for enabling high performance devices—a task which relies on a good understanding of their crystallization pathways [29–31].

The present study aims to reveal the formation of 2D perovskite compositions, based on a monofunctional 2-phenyethylammonium (PEA^+) spacer cation, often used for passivation of the perovskite surface [32–34]. We explore the target dimensionalities $\bar{n} = 1 - 3$, as well as different small cations (MA^+ or FA^+), and halides (Br^- or I^-).

2. Experiment

Perovskite thin films of different compositions were prepared by spin-coating 40 µL of 0.4 M precursor solution containing MAI/MABr or FAI/FABr, PEAI/PEABr and PbI_2/$PbBr_2$ in two stages (1000 rpm for 10 s followed by 4000 rpm for 30 s) on plasma-cleaned indium tin oxide (ITO) coated 10×10 mm^2 glass substrate in nitrogen atmosphere. The precursors had molar ratios corresponding to the target perovskite dimensionality ($\bar{n} = 1$, $\bar{n} = 2$ and $\bar{n} = 3$) and were dissolved in a mixture of N,N-dimethylformamide (DMF) and dimethyl sulfoxide (DMSO) with 4:1 volume ratio. The perovskite crystallization was induced by thermal annealing with an infrared (IR) lamp, during which the temperature was recorded by a pyrometer.

To track the formation of the 2D perovskites from the precursor solutions by *in situ* GIWAXS, the samples were fabricated in a custom-built spin-coater [35]. This spin-coater features two Kapton windows for X-rays and has a specially designed spinning stage, which is compatible with *in situ* diffraction studies in grazing incidence geometry [36]. GIWAXS is a non-destructive and surface sensitive technique ideally suited for perovskite thin film studies [30,31,37–43] as it allows *in situ* tracking of the formation and degradation of perovskite structures and the determination of the crystal orientation, crystallographic texture and strain [5,44–46]. The experiment was performed at the P08 beamline of the PETRA III synchrotron [47]. The X-ray beam with energy $E = 18$ keV had a size 0.1 mm $\times$ 0.4 mm (vert. $\times$ hor.) and an incidence angle $\alpha_i = 0.5°$ to the sample surface. The scattered intensity was recorded with a 0.1 s exposure time by a Perkin Elmer detector (XRD 1621 CN3 EHS, 2048 $\times$ 2048 pixels) positioned at a distance $D = 0.77$ m (for iodide compositions) or $D = 0.712$ m (for bromide compositions) from the sample. Directly after the sample preparation, we performed GIWAXS measurements with varying angle of incidence α_i. Due to the high roughness and absorption of the film, the general trend is that the scattered intensity increases with the incidence angle. However, the slope is different, which allowed us to get insights into the stacking order of different phases. In addition we measured diffraction scans in specular reflection geometry to get insights into the structure in the direction perpendicular to the substrate. The q-range along the vertical axis, probed by the specular scans, is inaccessible in the GIWAXS geometry due to the so-called missing wedge [45,46].

The Bragg reflections in the GIWAXS data were indexed by simulating the diffraction patterns of expected 2D perovskite structures based on Crystallographic Information Files (CIF) from the 2D perovskite database [48]. This allowed the identification of the existing crystal structures as well as their orientation with respect to the substrate [49]. The crystallization kinetics of different perovskite phases was evaluated by integrating the intensity of prominent Bragg peaks as a function of time. For this we selected up to five most prominent peaks belonging to a certain phase, integrated the intensity of these peaks, normalized the acquired time-dependencies and averaged the result to obtain an adequate estimate the relative change of the amount of this phase in the sample. Selecting a larger number of diffraction peaks for this type of analysis did not necessarily lead to a better result, because of the low signal-to-noise ratio at higher $|q|$ and due to the presence of the missing wedge.

3. Results and Discussion

3.1. Samples with Iodide Anion

In the case of samples with iodide anion, the precursor solution crystallizes into perovskite phases only upon thermal annealing, no crystallization is taking place during the spin-coating process. The observed crystal structures and their parameters are listed in Table 1. *Ex situ* GIWAXS data and specular scans recorded for the samples with iodide anion, indexed with the observed crystal structures, are displayed in Figure 2. The positions and intensity of the peaks were calculated from the crystallographic data in the CIF files given in Table 1 using the available package `crystals` [50] and own code to overlay it with the experimental GIWAXS data.

Table 1. Crystal structures observed for the samples with iodide anion and their corresponding unit cell parameters. References to the used CIF files are provided. The unit cell of the FA-based 2D perovskite was obtained based on the available MA-based CIF file. In the absence of any structural information, we assumed that the c-axis of α and β polymorphs is perpendicular to the substrate.

Phase	a [Å]	b [Å]	c [Å]	α [deg]	β [deg]	γ [deg]
PEA_2PbI_4 ($n = 1$) [51]	8.7389(2)	8.7403(2)	32.9952(6)	84.6460(10)	84.6570(10)	89.6430(10)
α polymorph	-	-	25.88	-	-	-
β polymorph	-	-	21.00	-	-	-
$PEA_2MAPb_2I_7$ ($n = 2$) [52]	8.8092(5)	8.168(4)	22.8196(12)	97.072(4)	93.983(4)	90.199(4)
$PEA_2FAPb_2I_7$ ($n = 2$)	8.8	8.8	22.8	97.1	94.0	90.2
$MAPbI_3$ [53]	6.3115(2)	6.3115(2)	6.3161(2)	90	90	90
$FAPbI_3$ [54]	6.3691(2)	6.3691(2)	6.3691(2)	90	90	90
$FAPbI_3$ δ-phase [53]	8.6667(6)	8.6667(6)	7.9077(6)	90	90	120

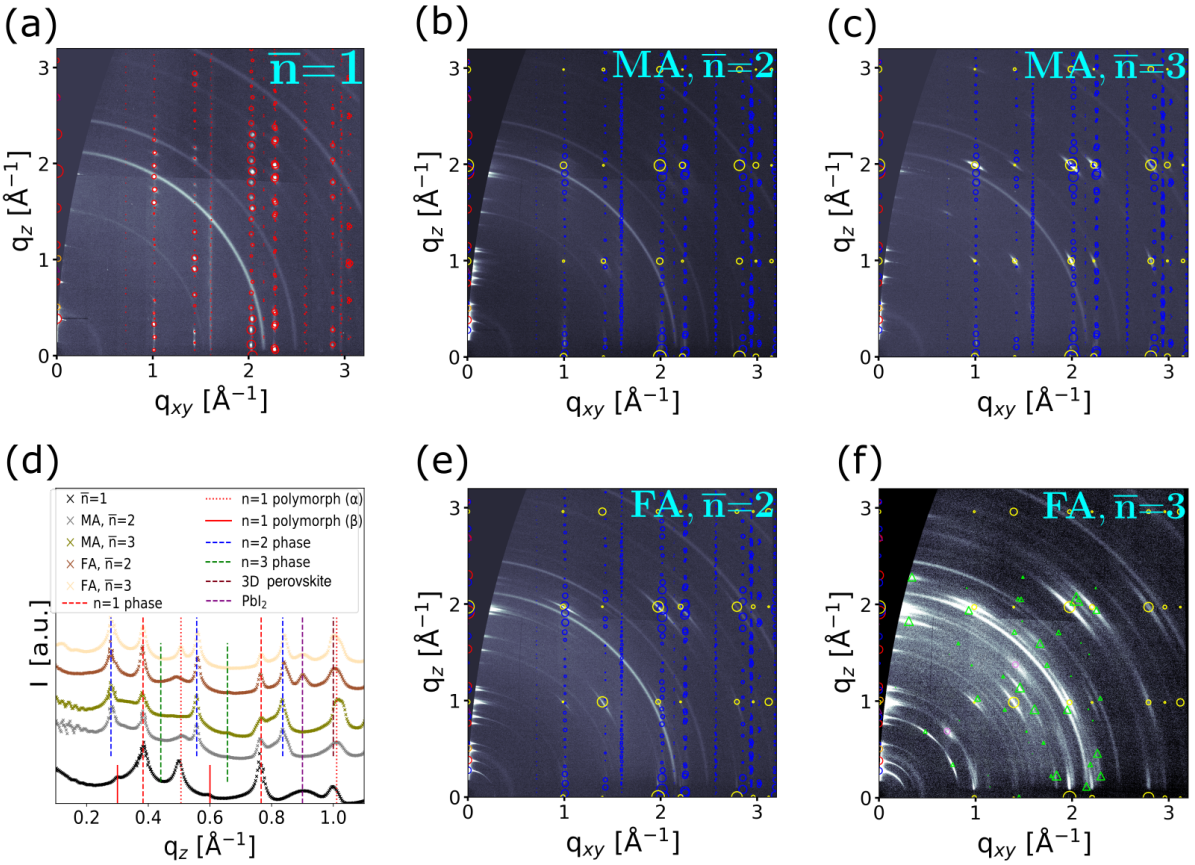

Figure 2. GIWAXS data and specular scans of the samples with iodide anion: (**a**) GIWAXS data for the sample with $\bar{n} = 1$ target dimensionality, (**b**) GIWAXS data for the sample with $\bar{n} = 2$ target dimensionality and MA^+ cation, (**c**) GIWAXS data for the sample with $\bar{n} = 3$ target dimensionality and MA^+ cation, (**d**) specular scans for all the samples, (**e**) GIWAXS data for the sample with $\bar{n} = 2$ target dimensionality and FA^+ cation, (**f**) GIWAXS data for the sample with $\bar{n} = 3$ target dimensionality and FA^+ cation. On the GIWAXS data, the horizontally oriented $n = 1$ phase is marked with red circles (o), the $n = 1$ α polymorph is marked with orange circles (o), the horizontally oriented $n = 2$ phase is marked with blue circles (o), the 3D perovskite phase is marked with yellow circles (o) or with pink circles (o) for the tilted orientation, the $FAPbI_3$ δ-phase is marked with light green triangles (△) and the lead iodide is marked with a violet triangle (△). The size of the markers is proportional to the intensity of the corresponding simulated diffraction peaks.

The sample with $\bar{n} = 1$ target dimensionality (Figure 2a) crystallizes predominantly into the $n = 1$ (PEA_2PbI_4) Ruddlesden-Popper layered perovskite structure [51]. The (001) plane of the unit cell is oriented parallel to the substrate, which corresponds to horizontal orientation of the perovskite layers, when the 2D planes formed by interconnected PbI_6 octahedra are parallel to the substrate (see Figure 1b,c). The observed Bragg peaks are very narrow (≤ 0.01 Å^{-1}), suggesting a large size of crystal grains with a high degree of orientational order. We observe that the peaks exhibit vertical streaking (crystal truncation rod—like features) which is often found for 2D perovskites [45]. The specular scan has two additional pairs of peaks which reveal the existence of two possible $n = 1$ polymorphs which we name the α polymorph (having the long axis $c^{\alpha} = 25.88$ Å, also visible in the $\bar{n} > 1$ samples), and the β polymorph (having the long axis $c^{\beta} = 21.00$ Å, visible only in the $\bar{n} = 1$ sample). The length of the c lattice parameters for both polymorphs is smaller than the corresponding value of the $n = 1$ phase value ($c = 32.82$ Å), suggesting a smaller number of PEA^+ spacers in the polymorphs, or a different orientation with the spacer cation more parallel to the substrate. Partial loss of the spacer cation can lead to improved power conversion efficiency of the perovskite solar cell [55]. Additionally, a surplus of lead iodide (PbI_2) is indicated by the peak at q_z = 0.9 Å^{-1} [56].

The left column of panels in Figure 3 shows the intensity evolution of the different phases in the samples with iodide anion during their annealing. The right column in Figure 3 reveals the dependence of the phase intensity on the X-ray beam incidence angle, which corresponds to the probing depth inside the resulting film after annealing. We observe two different crystallization stages (Figure 3a). The first stage (∼5 s) is characterized by a sharp increase in the intensity of the $n = 1$ perovskite phase, while the second stage is characterized by a much slower subsequent linear increase of the peak intensity. The Bragg peak intensity of the β polymorph displays a sharp increase immediately after the start of annealing and reins constant until around $t = 200$ s, while the Bragg peak intensity of the α polymorph increases linearly. After $t = 200$ s, the α polymorph starts converting into the β polymorph until the end of annealing, after which the intensity of both polymorphs is increasing again.

For samples incorporating MA or FA (with $\bar{n} = 2$ or $\bar{n} = 3$ target dimensionality), mixtures of layered phases can be observed (Figure 2b-f). First, we can clearly distinguish the horizontally oriented $n = 1$ and $n = 2$ phases from the peaks along q_z (Figure 2d). Second, we also observe peaks corresponding to the 3D perovskite phase. These peaks are more pronounced for the samples with $\bar{n} = 3$ target dimensionality, as can be expected based on the composition.

From the data shown in Figure 3 we can draw the following key conclusions. First, for $\bar{n} = 3$ target dimentionality, the 3D perovskite phase (and $FAPbI_3$ δ-phase for FA-based sample) nucleate first and are located at the top of the film, which means that the crystallization process starts from the film surface. Second, for the FA-based sample with $\bar{n} = 2$ (Figure 3d,i) we do not observe the transformation of the hexagonal δ-phase into the 3D perovskite phase $FAPbI_3$ during the annealing, which is typical for the samples without spacer cations [30,57]. Apparently the PEA^+ spacer stabilizes the 3D perovskite phase which crystallizes directly from the solution. Only at the lower spacer concentration ($\bar{n} = 3$ sample shown in Figure 3e,j), we find a scenario where part of the precursor solution crystallizes into the hexagonal δ-phase and part of it crystallizes directly into the 3D perovskite phase.

The sample with FA^+ cation and $\bar{n} = 3$ target dimensionality has additional Bragg peaks corresponding to a different orientation of $FAPbI_3$, which is tilted by an angle $\tau = 45°$ with respect to the normal to the substrate along the horizontal $\langle 100 \rangle$ crystallographic directions. In this sample we also identified the $FAPbI_3$ δ-phase [58], which is tilted at an angle $\tau = 55°$ with respect to the normal to the substrate along the horizontal $\langle 210 \rangle$ crystallographic direction. For the FA-based samples, the 3D perovskite phase crystallizes faster than the 2D perovskite phases (Figure 3d,e), and forms on top of the film (Figure 3i,j), similar to the MA-based samples. Additionally, for the FA-based sample with $\bar{n} = 3$, the hexagonal δ-phase converts into 3D perovskite phase during the annealing procedure, while both FA samples show an increase of lead iodide over time which can be attributed to thermal decomposition of the perovskite phase. The 2D phases in the interior of the film are not involved in this interplay between the hexagonal δ-phase, 3D perovskite and PbI_2, which all coexist at the top of the film.

A very small amount of horizontally oriented $n = 3$ phase is formed in the MA $\bar{n} = 3$ sample (visible from the small peak in the specular scan), but is absent in the FA $\bar{n} = 3$ sample. The absence of $n > 2$ phases in the FA-based samples, is expected due to the structural properties of the composition, which crystallizes into $FAPbI_3$ δ-phase instead, as was also observed in other studies [59]. A general trend is that the peaks become broader in the azimuthal direction when increasing the target dimensionality of the samples $\bar{n}$, which corresponds to a lower orientational order of the crystal structures.

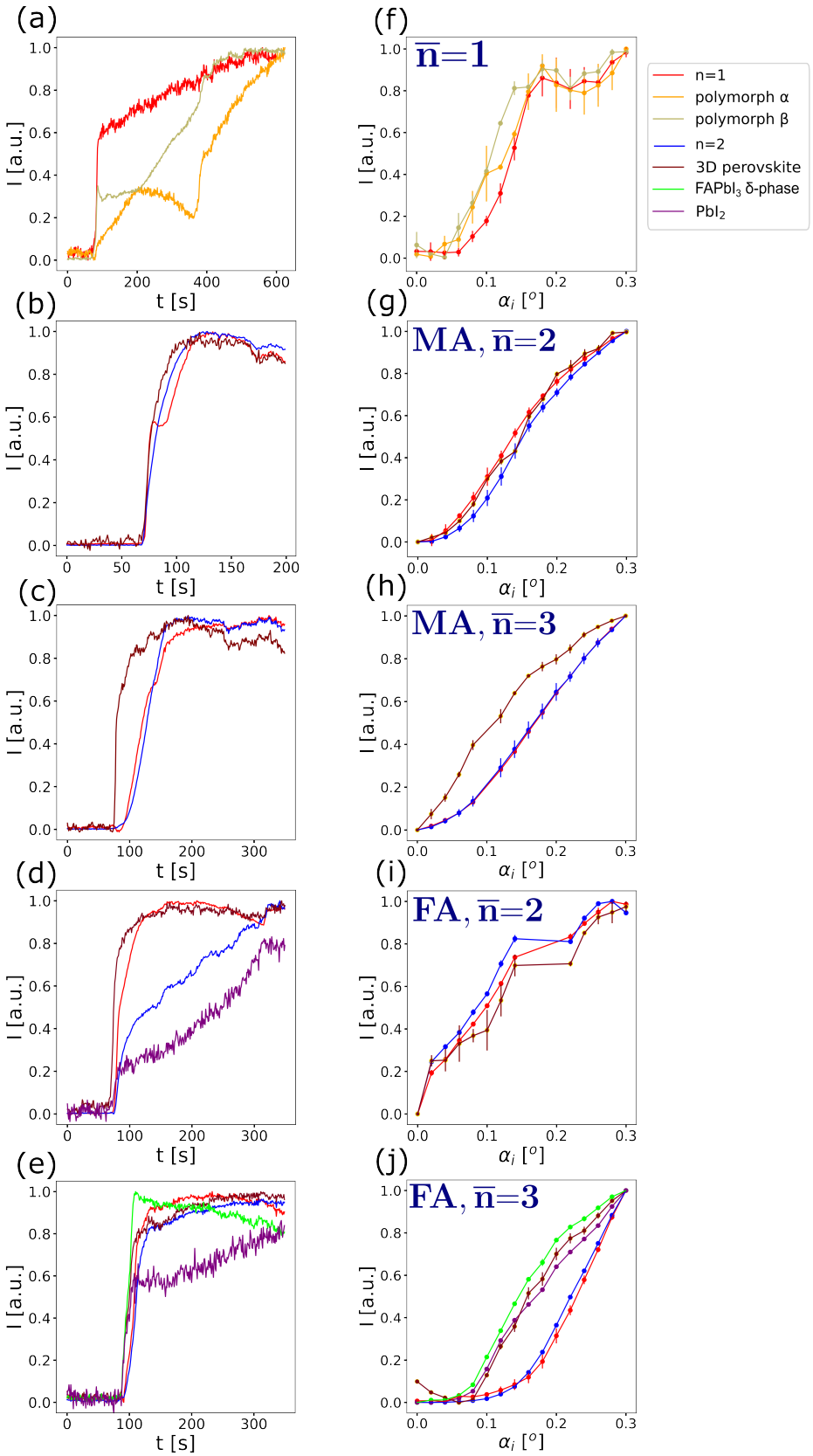

Figure 3. (**a**–**e**) Intensity evolution of the different crystal phases for samples with iodide anion during the process of thermal annealing. The normalized intensity of each phase is illustrated by a continuous line. (**f**–**j**) Normalized intensities of the phases present in the sample as a function of the angle of incidence of the beam on the finished sample after annealing. The critical angle of the 2D perovskite phases is $\alpha_{C,2D} \approx 0.095^{\circ}$ and the critical angle of the 3D phases is $\alpha_{C,3D} \approx 0.115^{\circ}$.

3.2. Samples with Bromide Anion

In the case of the samples with bromide anion, the precursor solution starts crystallizing into perovskite phases already during spin-coating and continues during the thermal annealing, similar to the 3D perovskites with bromide anion [42]. This behavior is qualitatively different from the samples with iodide anion. GIWAXS data together with their radially integrated profiles for the samples with bromide anion, indexed with the observed crystal structures, are displayed in Figure 4. The specular scans were not measured for the bromide samples due to the absence of polymorphs. The crystal lattice parameters for the bromide-based compositions are summarized in Table 2. Figure 5 shows the intensity evolution (left column) of the different phases in the samples with bromide anion during spin-coating (regions before the thick vertical line) and annealing (region after the thick vertical line), as well as the dependence of the phase intensity on the incidence angle of the beam (right column), which corresponds to the probing depth inside the film.

Table 2. Crystal structures observed for the samples with bromide anion and their corresponding unit cell parameters. References to the used CIF files are provided. The unit cell of the $n = 2$ perovskite phase was determined by authors from the recorded GIWAXS data.

Phase	a [Å]	b [Å]	c [Å]	α [deg]	β [deg]	γ [deg]
PEA_2PbBr_4 ($n = 1$) [60]	11.6150(4)	11.6275(5)	17.5751(6)	99.5472(12)	105.7245(10)	89.9770(12)
$PEA_2MAPb_2Br_7$ ($n = 2$)	8.19	8.2	22.82	97.07	93.98	90.2
$PEA_2FAPb_2Br_7$ ($n = 2$)	8.2	8.2	22.9	97.1	94.0	90.2
$MAPbBr_3$ [61]	5.9328(14)	5.9328(14)	5.9328(14)	90	90	90
$FAPbBr_3$ [62]	5.9968(7)	5.9968(7)	5.9968(7)	90	90	90

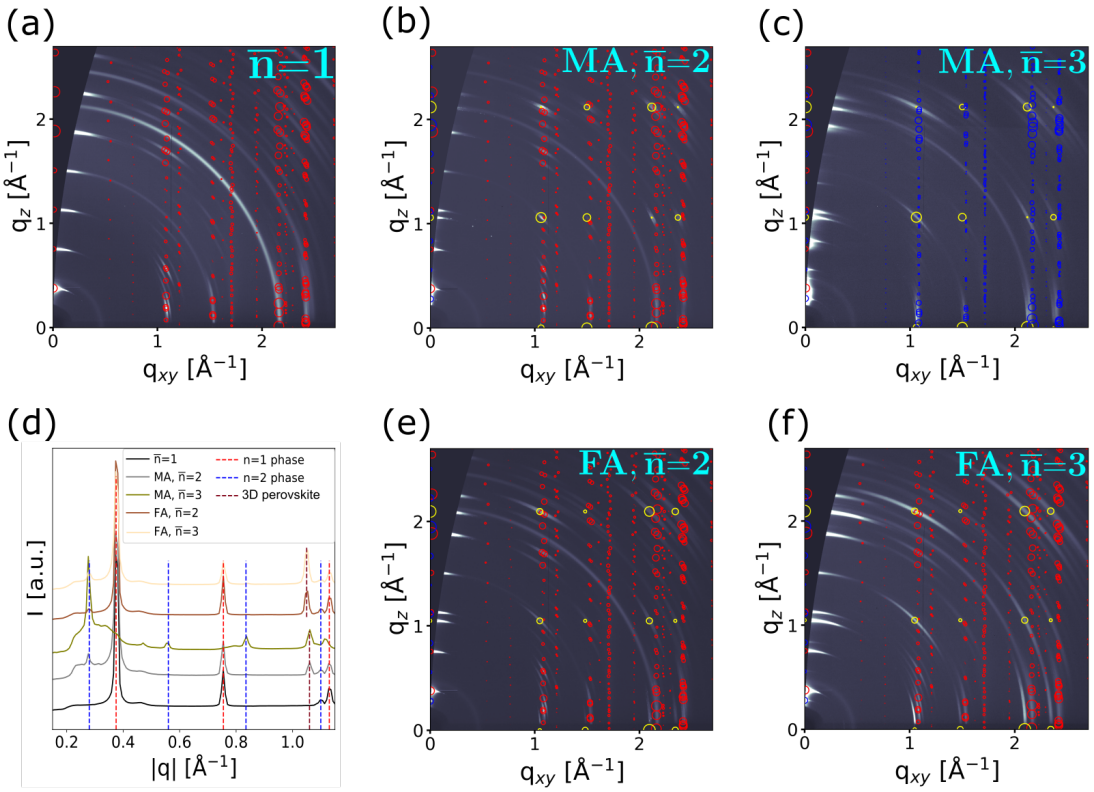

Figure 4. GIWAXS data and the corresponding radially integrated profiles of the samples with bromide anion: (**a**) GIWAXS data for the sample with $\bar{n} = 1$ target dimensionality, (**b**) GIWAXS data for the sample with $\bar{n} = 2$ target dimensionality and MA^+ cation, (**c**) GIWAXS data for the sample with $\bar{n} = 3$ target dimensionality and MA^+ cation, (**d**) radially integrated profiles for all the samples, (**e**) GIWAXS data for the sample with $\bar{n} = 2$ target dimensionality and FA^+ cation, (**f**) GIWAXS data for the sample with $\bar{n} = 3$ target dimensionality and FA^+ cation. On the GIWAXS data, the horizontally oriented $n = 1$ phase is marked with red circles (o), the horizontally oriented $n = 2$ phase is marked with blue circles (o) and the 3D perovskite phase is marked with yellow circles (o). The size of the markers is proportional to the intensity of the corresponding simulated diffraction peaks.

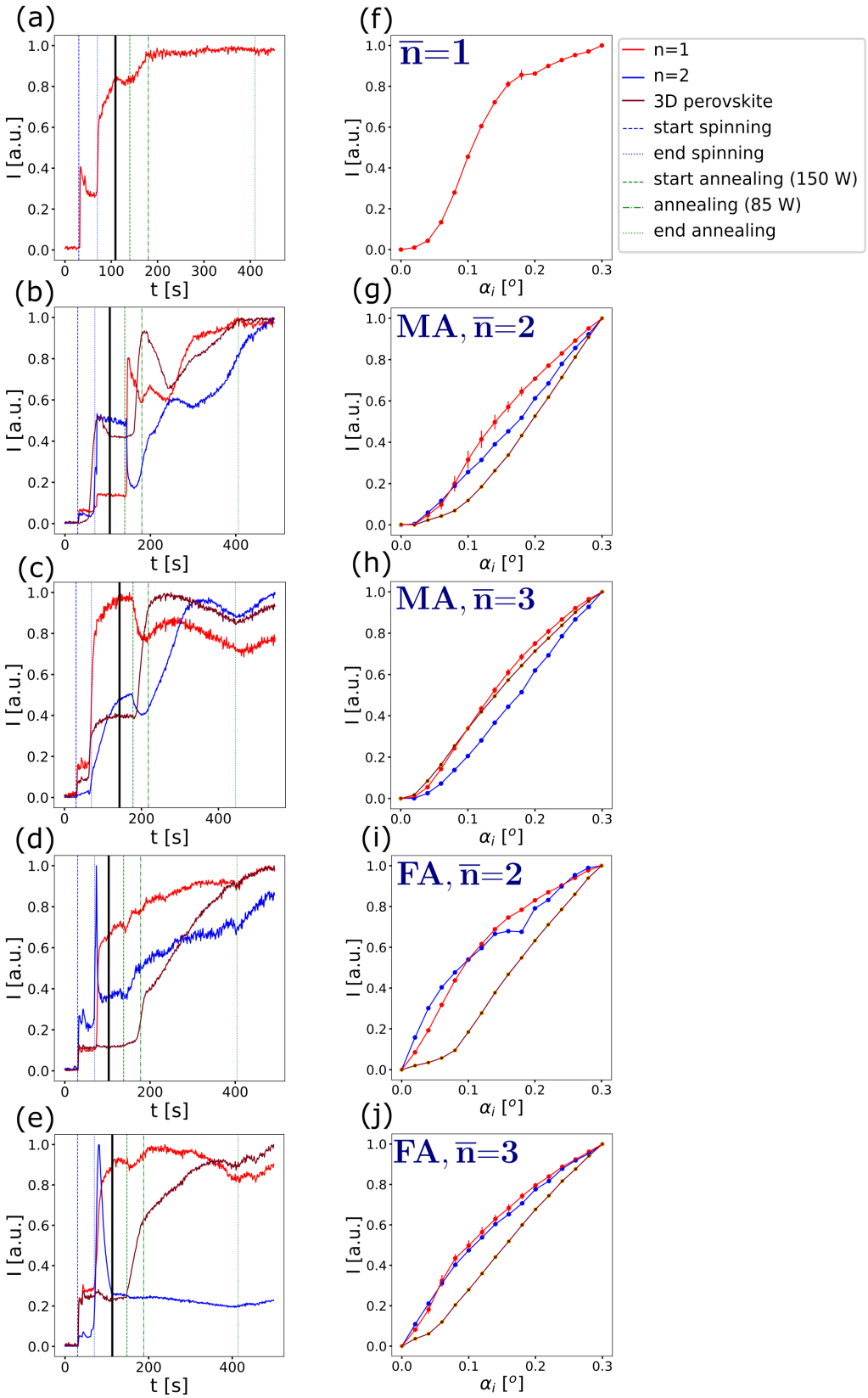

Figure 5. (**a**–**e**) Intensity evolution of the different crystal phases for samples with bromide anion during the spinning and annealing. The normalized intensity of each phase is shown by solid lines. The vertical lines represent different stages of film fabrication: the black solid line separates the spinning and the annealing measurements, the blue dashed and dotted lines indicate the start and end of spinning, respectively; the green dashed, dot-dash and dotted lines indicate the start of annealing (at 150 W of the IR lamp), reducing the power of the annealing IR lamp to 85 W, and the end of annealing, respectively. (**f**–**j**) Normalized intensities of the phases as a function of the X-ray beam angle of incidence. The critical angle of the 2D perovskite phases is $\alpha_{C,2D} \approx 0.095^{\circ}$ and the critical angle of the 3D phases is $\alpha_{C,3D} \approx 0.115^{\circ}$.

The sample with $\bar{n} = 1$ target dimensionality (Figure 4a) crystallizes into the $n = 1$ (PEA_2PbBr_4) Ruddlesden-Popper layered perovskite structure with predominantly horizontal orientation (see Figure 1b). Here, the Bragg peaks are much broader compared to the $\bar{n} = 1$ sample with iodide anion, which indicates that the crystalline grains have a broad distribution of orientations centered around the preferred horizontal orientation. Figure 5a shows that the $n = 1$ phase forms already during spin-coating and only a relatively small amount crystallizes during annealing. A steep increase in intensity immediately after the spinning stops might be caused by a small displacement of the substrate in vertical direction, which can increase the X-ray footprint on the sample.

For samples incorporating MA or FA (with $\bar{n} = 2$ or $\bar{n} = 3$ target dimensionality), we observe the existence of the $n = 1$ and $n = 2$ 2D perovskite phases with horizontal orientation and the 3D perovskite phase. In the $\bar{n} = 2$ MA-based composition and in both FA-based samples, the intensity of the Bragg peaks suggests a larger amount of $n = 1$ phase compared to $n = 2$ phase in these samples. Conversely, in the $\bar{n} = 2$ MA-based composition, the majority phase is $n = 2$ instead of $n = 1$. The 3D perovskite phase ($MAPbBr_3$ or $FAPbBr_3$, depending on the composition) is present in all the $\bar{n} > 1$ samples, similar to the iodide samples. Also, similar to the samples with iodide anion, the broadening of the peaks signifies more random orientation of the crystal structure when increasing the target dimensionality $\bar{n}$.

The intensity evolution of the distinct crystal phases in the bromide samples (Figure 5, left column) is more complex compared to the iodide samples, but some general trends can still be observed. The 2D phase with $n = 1$ tends to form predominately during spin-coating and further crystallizes during annealing, as it can be seen for the $\bar{n} = 3$ MA composition and all FA compositions. On the other hand, while the 3D perovskite phase starts forming during spin-coating, it crystallizes mostly during annealing, which is especially apparent for the FA samples.

While for the iodide samples the 3D phase tends to form predominantly on the top of the film and the 2D phases towards the bottom, this trend is inverted for the bromide samples. Here the 2D phases tend to form close to the surface of the film while the 3D phase tends to form closer to the substrate (Figure 5, right column).

These results can be attributed to the intrinsic differences in the chemical and physical properties of the iodide and bromide ions, which affect the crystallization process of the different phases in perovskite films. For the iodide-based samples, the crystallization takes place during annealing and it starts from the top, since the substrate is also heated from the top by an IR lamp. In this process, the 3D perovskite phase is predominantly formed on the top of the film, while 2D phases are formed below. For the bromide-based samples, the crystallization of the 2D phases starts already during spin-coating.

4. Conclusions

In this study, we investigated the crystallization process of 2D perovskite thin films with 2-phenyethylammonium (PEA^+) spacer cation upon spin-coating and thermal annealing from precursor solutions with various compositions (iodide or bromide anion, MA^+ or FA^+ small organic cation and $\bar{n}$ = 1, 2 or 3 target dimensionality). Using the GIWAXS data, we determined the unit cell parameters for several $n = 2$ phases of 2D perovskites, namely, $PEA_2FAPb_2I_7$, $PEA_2FAPb_2Br_7$ and $PEA_2MAPb_2Br_7$.

The thin films displayed a mixture of coexisting phases depending on the employed precursor composition. The visual summary of the different phases in the final samples is given in Figure 6. Generally, the higher the target dimensionality, the higher the degree of orientational disorder of the obtained crystal structures.

The resulting horizontally oriented 2D perovskite phases are located on top of the 3D perovskite phase for three out of the four $\bar{n} > 1$ bromide-based samples. This stacking order is preferable for the applications in solar cells, since the 2D perovskite can then potentially protect the 3D perovskite from environmental degradation factors.

We also determined that the choice of anion plays a crucial role in terms of the perovskite crystallization pathways. For the iodide anion, the perovskite structures crystallize only during annealing. In contrast, when the bromide anion is used, the perovskite structures start crystallizing already during spin-coating and further crystallize during annealing. For the bromide samples, the crystallization pathways are also more complex, revealing the mutual conversion between the perovskite phases during the crystallization process. Also bromide-based samples exhibit significantly less polymorphism compared to the iodide-based samples.

For the iodide samples, we observed the general trend that the structures which are distributed towards the top surface of the film also crystallize faster. This indicates that the crystallization process starts from the film surface, which might be caused by heating the samples with an IR lamp from the top during the annealing. It is important that the 3D perovskite phase (and δ-phase) crystallize before the 2D phases which means that they are more energetically favorable. This may prevent the formation of higher $n = 3$ phases which would happen at higher annealing temperatures.

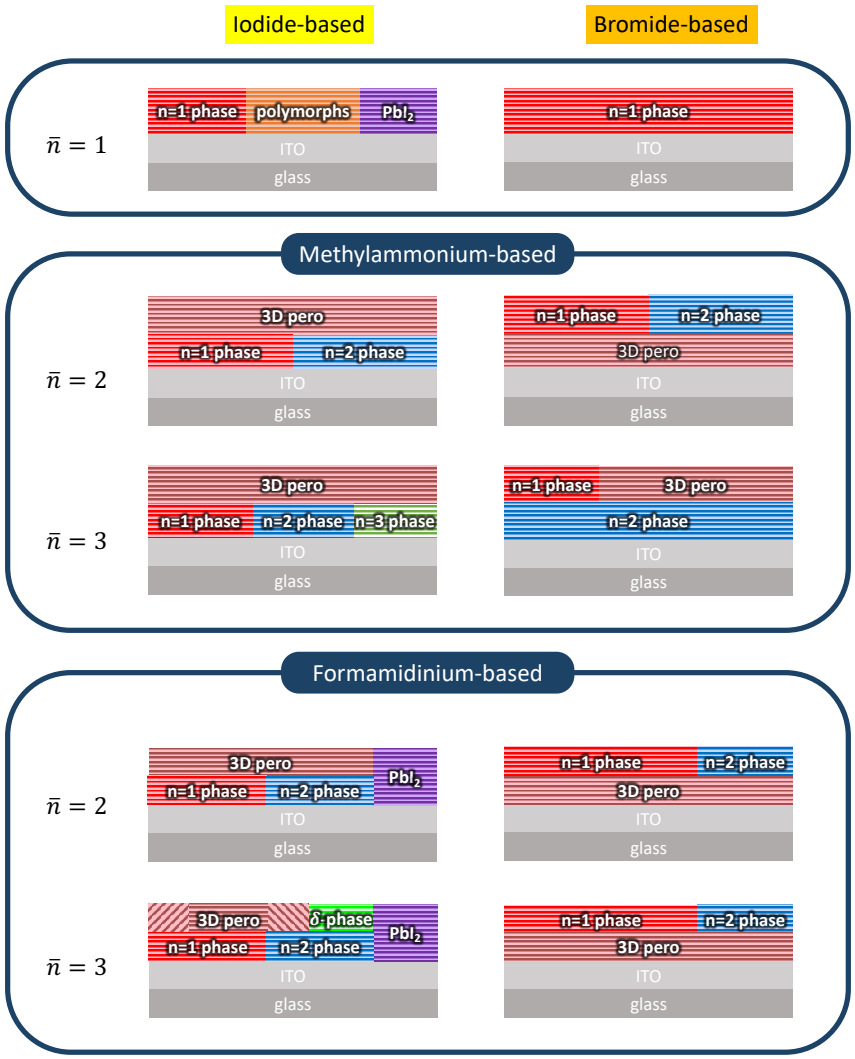

Figure 6. Visual summary of the crystalline phases coexisting in thin films: 2D perovskites with $n = 1, 2, 3$, 3D perovskites, δ-phase of $FAPbI_3$, PbI_2 and α- and β-polymorphs. Each schematic represents the phases observed in the sample and the proposed stacking order and the predominant orientation of the phases (importantly, the horizontal orientation of the 2D phases).

In conclusion, the X-ray *in situ* investigations provide important insight into the formation mechanisms of two-dimensional halide perovskites during spin-coating. The crystallization pathways are strongly governed by the chemical composition, including the choice of A-site cation and halide anion. While we focused here on 2D phases formed with PEA^+ cation, there is a large number of other organic spacers that could be used to fabricate a 2D perovskite phase with desired structure and photovoltaic properties. A deeper understanding of crystallization scenarios, enabled by *in situ* methodologies, provides a pathway toward the rational design of robust high-performance optoelectronic devices based on 2D perovskites.

Supplementary Materials

The additional data and information can be downloaded at: https://media.sciltp.com/articles/others/260408134156123 9/MatSus-26020066-SI-FC.pdf. Figure S1: Colormaps of $I(q, t)$ for the *In-situ* GIWAXS patterns from the samples with different cations (MA^+ or FA^+) and target dimensionalities $\bar{n} = 1, 2, 3$. Left column shows annealing of the iodide-based samples and right column shows spinning and annealing of the bromide-based samples. Figure S2: *Ex-situ* GIWAXS patterns from the samples with iodide anion with different cations (MA^+ or FA^+) and target dimensionalities $\bar{n} = 1, 2, 3$. Left column shows data measured at the incidence angle $\alpha_{in} = 0.1°$ and right column at $\alpha_{in} = 0.2°$. Figure S3: *Ex-situ* GIWAXS patterns from the samples with bromide anion with different cations (MA^+ or FA^+) and target dimensionalities $\bar{n} = 1, 2, 3$. Left column shows data measured at the incidence angle $\alpha_{in} = 0.1°$ and right column at $\alpha_{in} = 0.2°$.

Author Contributions

V.M.: measurements, data analysis, visualization, writing; E.K.: measurements, data analysis, visualization, writing; L.M.: measurements, writing; A.D.: sample preparation; J.M.: conceptualization, sample preparation, editing, supervision; F.B.: measurements; A.H.: conceptualization, writing, supervision; A.G.: conceptualization, supervision; I.Z.: visualization, writing, supervision; F.S.: conceptualization, reviewing, editing, supervision. All authors have read and agreed to the published version of the manuscript.

Fundung

We acknowledge funding from the BMBF (ERUM-Pro) project 05K19VTA.

Institutional Review Board Statement

Not applicable.

Informed Consent Statement

Not applicable.

Data Availability Statement

The data that support the findings of this study are available from the corresponding author upon reasonable request.

Acknowledgments

We acknowledge DESY (Hamburg, Germany), a member of the Helmholtz Association HGF, for the provision of experimental facilities. Parts of this research were carried out at P08 beamline of at PETRA III. Beamtimes were allocated for proposals I-20190761 and I-20200254. We acknowledge the LISA+ Center at the University of Tübingen for technical support

Conflicts of Interest

The authors declare no conflict of interest.

Use of AI and AI-Assisted Technologies

There is no AI or AI-assisted technology used in this article.

References

1. Green, M.A.; Ho-Baillie, A.; Snaith, H.J. The emergence of perovskite solar cells. *Nat. Photon.* **2014**, *8*, 506–514.
2. Park, N.G. Perovskite solar cells: An emerging photovoltaic technology. *Mater. Today* **2015**, *18*, 65–72.
3. Snaith, H.J. Present status and future prospects of perovskite photovoltaics. *Nat. Mater.* **2018**, *17*, 372–376.
4. Biegel, C.M. Perovskite Stories from Around the World. *ACS Energy Lett.* **2019**, *4*, 879–887.
5. Schmidt-Mende, L.; Dyakonov, V.; Olthof, S.; et al. Roadmap on organic-inorganic hybrid perovskite semiconductors and devices. *APL Mater.* **2021**, *9*, 109202.
6. Maqsood, A.; Näsström, H.; Chen, C.; et al. Towards an interoperable perovskite description or how to keep track of 300 perovskite ions. *Nat. Commun.* **2025**, *16*, 8725.
7. Kojima, A.; Teshima, K.; Shirai, Y.; et al. Organometal Halide Perovskites as Visible-Light Sensitizers for Photovoltaic Cells. *J. Am. Chem. Soc.* **2009**, *131*, 6050–6051.
8. Stranks, S.D.; Eperon, G.E.; Grancini, G.; et al. Electron-Hole Diffusion Lengths Exceeding 1 Micrometer in an Organometal Trihalide Perovskite Absorber. *Science* **2013**, *342*, 341–344.
9. Johnston, M.B.; Herz, L.M. Hybrid Perovskites for Photovoltaics: Charge-Carrier Recombination, Diffusion, and Radiative Efficiencies. *Acc. Chem. Res.* **2015**, *49*, 146–154.
10. Snaith, H.J. Perovskites: The Emergence of a New Era for Low-Cost, High-Efficiency Solar Cells. *J. Phys. Chem. Lett.* **2013**, *4*, 3623–3630.
11. Gielen, D.; Boshell, F.; Saygin, D.; et al. The role of renewable energy in the global energy transformation. *Energy Strateg. Rev.* **2019**, *24*, 38–50.
12. Jiang, W.; Qu, G.; Huang, X.; et al. Toughened self-assembled monolayers for durable perovskite solar cells. *Nature* **2025**, *646*, 95.

13. Tan, H.; Jain, A.; Voznyy, O.; et al. Efficient and stable solution-processed planar perovskite solar cells via contact passivation. *Science* **2017**, *355*, 722–726.
14. Hu, Y.; Niu, T.; Liu, Y.; et al. Flexible Perovskite Solar Cells with High Power-Per-Weight: Progress, Application, and Perspectives. *ACS Energy Lett.* **2021**, *6*, 2917–2943.
15. Brinkmann, K.O.; Becker, T.; Zimmermann, F.; et al. Perovskite–organic tandem solar cells with indium oxide interconnect. *Nature* **2022**, *604*, 280.
16. Pearson, A.J.; Eperon, G.E.; Hopkinson, P.E.; et al. Oxygen Degradation in Mesoporous $Al_2O_3/CH_3NH_3PbI_{3-x}Cl_x$ Perovskite Solar Cells: Kinetics and Mechanisms. *Adv. Energy Mater.* **2016**, *6*, 1600014.
17. Niu, G.; Guo, X.; Wang, L. Review of recent progress in chemical stability of perovskite solar cells. *J. Mater. Chem. A* **2015**, *3*, 8970–8980.
18. Ortiz-Cervantes, C.; Carmona-Monroy, P.; Solis-Ibarra, D. Two-Dimensional Halide Perovskites in Solar Cells: 2D or not 2D? *ChemSusChem* **2019**, *12*, 1560–1575.
19. Milić, J.V. Multifunctional layered hybrid perovskites. *J. Mater. Chem. C* **2021**, *9*, 11428–11443.
20. Loizos, M.; Rogdakis, K.; Luo, W.; et al. Resistive switching memories with enhanced durability enabled by mixed-dimensional perfluoroarene perovskite heterostructures. *Nanoscale Horiz.* **2024**, *9*, 1146.
21. Luo, W.; Kim, J.M.; Zimmermann, P.; et al. Perfluoroarene-Based 2D/3D Perovskite Solar Cells. *ACS Appl. Energy Mater.* **2025**, *8*, 8914.
22. Liu, Y.; Akin, S.; Pan, L.; et al. Ultrahydrophobic 3D/2D fluoroarene bilayer-based water-resistant perovskite solar cells with efficiencies exceeding 22%. *Sci. Adv.* **2019**, *5*, eaaw2543.
23. Milić, J.V.; Zakeeruddin, S.M.; Grätzel, M. Layered Hybrid Formamidinium Lead Iodide Perovskites: Challenges and Opportunities. *Acc. Chem. Res.* **2021**, *54*, 2729–2740.
24. AlSabeh, G.; Slama, V.; Almalki, M.; et al. On the Accessibility of Higher-n Phases in Formamidinium-Based Ruddlesden-Popper and Dion–Jacobson Layered Hybrid Perovskites. *Adv. Electron. Mater.* **2025**, *11*, e00164.
25. Wali, Q.; Iftikhar, F.J.; Khan, M.E.; et al. Advances in stability of perovskite solar cells. *Org. Electron.* **2020**, *78*, 105590.
26. Scardina, A.; Loeff, T.F.; Vikram, V.; et al. Spacer Cation Design: Promoting Vertical Orientation in Layered Perovskites. *EES Sol.* **2026**. https://doi.org/10.1039/d6el00006a.
27. Chen, A.Z.; Shiu, M.; Ma, J.H.; et al. Origin of vertical orientation in two-dimensional metal halide perovskites and its effect on photovoltaic performance. *Nat. Commun.* **2018**, *9*, 1336.
28. Sun, K.; Guo, R.; Liu, S.; et al. Deciphering Structure and Charge Carrier Behavior in Reduced-Dimensional Perovskites. *Adv. Funct. Mater.* **2024**, *34*, 2411153.
29. Moore, D.T.; Sai, H.; Tan, K.W.; et al. Crystallization Kinetics of Organic–Inorganic Trihalide Perovskites and the Role of the Lead Anion in Crystal Growth. *J. Am. Chem. Soc.* **2015**, *137*, 2350–2358.
30. Buyan-Arivjikh, A.; Fricker, J.; Baier, T.; et al. $CsPbBr_3$ Nanocrystals as Bottom Interface Nucleation Seeds for Printing Oriented $FAPbI_3$ Thin Films: An *In Situ* Study. *Small* **2025**, *21*, e05895.
31. Liang, D.; Dong, C.; Cai, L.; et al. Unveiling Crystal Orientation in Quasi-2D Perovskite Films by *In Situ* GIWAXS for High-Performance Photovoltaics. *Small* **2021**, *17*, 2100972.
32. Li, C.; Chen, X.; Jin, T.; et al. Impact of functional groups in spacer cations on the properties of PEA-based 2D monolayer halide perovskites. *Nano Mater. Sci.* **2025**, *7*, 74–82.
33. Nishimura, N.; Kanda, H.; Katoh, R.; et al. Thermally stable phenylethylammonium-based perovskite passivation: Spontaneous passivation with phenylethylammonium bis(trifluoromethylsulfonyl)imide during deposition of PTAA for enhancing photovoltaic performance of perovskite solar cells. *J. Mater. Chem. A* **2024**, *12*, 15631.
34. Chen, R.; Gu, L.; Su, J.; et al. Stabilizing 2D perovskite passivation layer with mixed spacer cations for efficient and stable perovskite solar cells. *Nano Energy* **2025**, *139*, 110904.
35. Kneschaurek, E.; Hinderhofer, A.; Hofferberth, B.; et al. Compact sample environment for *in situ* X-ray scattering during spin-coating. *Rev. Sci. Instrum.* **2023**, *94*, 063901.
36. Hexemer, A.; Müller-Buschbaum, P. Advanced grazing-incidence techniques for modern soft-matter materials analysis. *IUCrJ* **2015**, *2*, 106–125.
37. Greco, A.; Hinderhofer, A.; Dar, M.I.; et al. Kinetics of Ion-Exchange Reactions in Hybrid Organic–Inorganic Perovskite Thin Films Studied by *In Situ* Real-Time X-ray Scattering. *J. Phys. Chem. Lett.* **2018**, *9*, 6750–6754.
38. Arora, N.; Greco, A.; Meloni, S.; et al. Kinetics and energetics of metal halide perovskite conversion reactions at the nanoscale. *Commun. Mater.* **2022**, *3*, 22.
39. Held, V.; Mrkyvkova, N.; Nádaždy, P.; et al. Evolution of Structure and Optoelectronic Properties During Halide Perovskite Vapor Deposition. *J. Phys. Chem. Lett.* **2022**, *13*, 11905–11912.
40. Antrack, T.; Kroll, M.; Merten, L.; et al. Enhancing Luminescence Efficiency by Controlled Island Formation of $CsPbBr_3$ Perovskite. *Adv. Opt. Mater.* **2022**, *11*, 2201408.
41. Telschow, O.; Scheffczyk, N.; Hinderhofer, A.; et al. Elucidating Structure Formation in Highly Oriented Triple Cation Perovskite Films. *Adv. Sci.* **2023**, *10*, 2206325.

42. Merten, L.; Eberle, T.; Kneschaurek, E.; et al. Halide Segregated Crystallization of Mixed-Halide Perovskites Revealed by *In Situ* GIWAXS. *ACS Appl. Mater. Interfaces* **2024**, *16*, 8913.
43. Maschwitz, T.; Merten, L.; Ünlü, F.; et al. How crystallization additives govern halide perovskite grain growth. *Nat. Commun.* **2025**, *16*, 9894.
44. Wang, C.; Zuo, C.; Chen, Q.; et al. GIWAXS: A powerful tool for perovskite photovoltaics. *J. Semicond.* **2021**, *42*, 060201.
45. Steele, J.A.; Solano, E.; Hardy, D.; et al. How to GIWAXS: Grazing Incidence Wide Angle X-Ray Scattering Applied to Metal Halide Perovskite Thin Films. *Adv. Energy Mater.* **2023**, *13*, 2300760.
46. Tan, W.L.; McNeill, C.R. X-ray diffraction of photovoltaic perovskites: Principles and applications. *Appl. Phys. Rev.* **2022**, *9*, 021310.
47. Seeck, O.H.; Deiter, C.; Pflaum, K.; et al. The high-resolution diffraction beamline P08 at PETRA III. *J. Synchrotron Radiat.* **2011**, *19*, 30–38.
48. Marchenko, E.I.; Fateev, S.A.; Petrov, A.A.; et al. Database of Two-Dimensional Hybrid Perovskite Materials: Open-Access Collection of Crystal Structures, Band Gaps, and Atomic Partial Charges Predicted by Machine Learning. *Chem. Mater.* **2020**, *32*, 7383–7388.
49. Smilgies, D.M. Probing Functional Thin Films with Grazing Incidence X-Ray Scattering: The Power of Indexing. *Crystals* **2025**, *15*, 63.
50. René de Cotret, L.P.; Otto, M.R.; Stern, M.J.; et al. An open-source software ecosystem for the interactive exploration of ultrafast electron scattering data. *Adv. Struct. Chem. Imag.* **2018**, *4*, 11.
51. Du, K.Z.; Tu, Q.; Zhang, X.; et al. Two-Dimensional Lead(II) Halide-Based Hybrid Perovskites Templated by Acene Alkylamines: Crystal Structures, Optical Properties, and Piezoelectricity. *Inorg. Chem.* **2017**, *56*, 9291–9302.
52. Song, J.; Dang, Y.; Liu, X.L.; et al. Layered hybrid lead perovskite single crystals: Phase transformations and tunable optical properties. *CrystEngComm* **2020**, *22*, 6310–6315.
53. Stoumpos, C.C.; Malliakas, C.D.; Kanatzidis, M.G. Semiconducting Tin and Lead Iodide Perovskites with Organic Cations: Phase Transitions, High Mobilities, and Near-Infrared Photoluminescent Properties. *Inorg. Chem.* **2013**, *52*, 9019–9038.
54. Huang, Y.; Li, L.; Liu, Z.; et al. The intrinsic properties of $FA_{(1-x)}MA_xPbI_3$ perovskite single crystals. *J. Mater. Chem. A* **2017**, *5*, 8537–8544.
55. Zhu, T.; Liu, M.; Cresp, M.; et al. Spacer Loss upon 2D Ruddlesden–Popper Halide Perovskite Annealing Raises Film Properties and Solar Cell Performances. *Nanomaterials* **2025**, *15*, 750.
56. Zhang, H.; Yu, W.; Guo, J.; et al. Excess PbI_2 Management via Multimode Supramolecular Complex Engineering Enables High-Performance Perovskite Solar Cells. *Adv. Energy Mater.* **2022**, *12*, 2201663.
57. Scheffczyk, N.; Kneschaurek, E.; Zimmermann, P.; et al. Lead Iodide Perovskite Thin Film Formation: The Impact of Preparation Method Studied by *In Situ* GIWAXS. *ACS Appl. Mater. Interfaces* **2025**, *17*, 67914.
58. Gratia, P.; Zimmermann, I.; Schouwink, P.; et al. The Many Faces of Mixed Ion Perovskites: Unraveling and Understanding the Crystallization Process. *ACS Energy Lett.* **2017**, *2*, 2686–2693.
59. Jahanbakhshi, F.; Mladenović, M.; Kneschaurek, E.; et al. Unravelling the structural complexity and photophysical properties of adamantyl-based layered hybrid perovskites. *J. Mater. Chem. A* **2020**, *8*, 17732–17740.
60. Shibuya, K.; Koshimizu, M.; Nishikido, F.; Saito, H.; et al. Poly[bis(phenethylammonium) [dibromidoplumbate(II)] -di-μ-bromido]]. *Acta Crystallogr. E* **2009**, *65*, m1323–m1324.
61. Jaffe, A.; Lin, Y.; Beavers, C.M.; et al. High-Pressure Single-Crystal Structures of 3D Lead-Halide Hybrid Perovskites and Pressure Effects on their Electronic and Optical Properties. *ACS Cent. Sci.* **2016**, *2*, 201–209.
62. Li, C.; Juarez-Perez, E.J.; Mayoral, A. Atomic-level understanding of a formamidinium hybrid halide perovskite, $FAPbBr_3$. *Chem. Commun.* **2022**, *58*, 12164–12167.